

In-silico molecular enrichment and clearance of the human intracranial space

Marius Causemann¹, Miroslav Kuchta¹, Rami Masri², and Marie E. Rognes^{1,3,*}

⁴¹Department of Numerical Analysis and Scientific Computing, Simula Research Laboratory, Oslo, Norway

⁵²Division of Applied Mathematics, Brown University, Providence, Rhode Island, USA

⁶³K. G. Jebsen Centre for Brain Fluid Research, University of Oslo, Norway

⁷*meg@simula.no

ABSTRACT

The mechanisms of intracranial solute transport are fundamental to human brain health, with alterations often linked to disease and functional impairment, and with distinct opportunities for personalized diagnostics and treatment. However, our understanding of these mechanisms and their interplay remains incomplete, in part due to the complexity of integrating insights across scales, between species and from different modalities. Here, we combine mixed-dimensional modelling, multi-modal magnetic resonance images, and high performance computing to construct and explore a high-fidelity in-silico model of human intracranial molecular enrichment. This model predicts the temporo-spatial spreading of a solute within an image-derived geometric representation of the subarachnoid space, ventricular system and brain parenchyma, including networks of surface perivascular spaces (PVSs). Our findings highlight the significant impact of cerebrospinal fluid (CSF) production and intracranial pulsatility on molecular enrichment following intrathecal tracer injection. We demonstrate that low-frequency vasomotion induces moderate CSF flow in surface PVS networks which substantially enhances tracer enrichment, and that impaired enrichment is a direct natural consequence of enlarged PVSs. This openly available technology platform thus provides an opportunity for integrating separate observations on diffusion in neuropil, vascular dynamics, intracranial pulsatility, CSF production, and efflux, and for exploring drug delivery and clearance in the human brain.

Introduction

The mechanisms underlying molecular transport within the intracranial space are fundamental to human brain health and function. Neurodegenerative diseases such as Alzheimer's, Parkinson's, and Huntington's disease are all associated with abnormal accumulation of protein aggregates together with alterations in transport and clearance characteristics^{1–4}. Moreover, sleep and conversely sleep-deprivation play a definite yet enigmatic role in modulating molecular enrichment and clearance^{5–9}. In the last decade, established theories have been challenged by new findings revealing a greater degree of molecular movement and exchange^{10–14}, as well as substantial variability in enrichment and clearance between individuals and between patient cohorts^{7,15–17}. These observations provide distinct opportunities (and challenges) for personalized medicine e.g. for tailored intrathecal delivery of chemotherapy¹⁸ and for early diagnostics of impaired brain clearance^{19,20}. In spite of their importance, our understanding of these mechanisms is incomplete with open challenges and significant debate – in part relating to the translation of knowledge between scales, species, experimental protocols, clinical cohorts, and individuals.

Perivascular pathways along the brain surface and within the brain parenchyma have long been hypothesized to serve a designated role in this context^{10,21–27}. Recently, Eide and Ringstad²⁸ and Yamamoto et al²⁹ demonstrated that perivascular spaces (PVSs) define preferential pathways for molecular transport in humans, with delayed periarterial enrichment in dementia subtypes²⁸. Perivascular flow of cerebrospinal fluid (CSF) clearly contributes to this transport, and is inherently associated with vascular pulsations^{30–35}. Fluid mechanics considerations point at intracranial pressure differences and shorter wavelength vascular wall pulsations as drivers of directional net flow and convection in the PVS^{36–41}, while longer waves such as the pulse wave primarily contribute to oscillatory flow and dispersion^{42–47}. In the bigger picture, CSF is produced by the choroid plexus^{48–50}, pulsates through the ventricular system, cisterns, and subarachnoid space (SAS) in synchrony with cardiac, respiratory, and neural waves^{16,51–58}, and drains via the dural sinuses, meningeal lymphatics, cranial nerves, or other efflux pathways¹³. However, how these physiological factors and physical mechanisms integrate to enhance or impair human intracranial molecular transport over larger spatial scales and longer time scales remain unknown. A related key question is to what extent surface PVSs are separated from the SAS by structural barriers^{22,28,59–64}, and in turn to what extent such structural compartmentalization is a prerequisite for effective perivascular transport.

In this study, by leveraging geometric model reduction and mixed-dimensional modelling⁶⁵, structural magnetic resonance (MR) images⁶⁶, and high performance computing, we introduce an integrated computational model of intracranial molecular

enrichment and clearance. Focusing on the interplay between perivascular pathways, pulsatility and CSF flow dynamics, the model predicts the temporal evolution and spatial distribution of a solute concentration within a detailed geometric representation of the human SAS and ventricular system, networks of surface PVSs and the brain parenchyma. In terms of transport dynamics, we account for heterogeneous diffusion, dispersive mixing induced by cardiac and respiratory pulsatility in the CSF spaces and PVSs, convective fluid flow driven by CSF production and peristaltic pumping, as well as solute exchange and clearance across semi-permeable membranes. Comparing with glymphatic MRI studies^{11,15,67}, the in-silico predictions accurately represent molecular enrichment patterns, timing and intercompartmental distributions. This open platform⁶⁸ thus provides a technological opportunity for qualitatively and quantitatively exploring key open questions relating to molecular movement within the human brain environment such as the role of pulsatility, perivascular pathways, structural compartmentalization, or morphology.

By exploring this high-dimensional parameter space, we propose that the balance between CSF production and intracranial pulsatility is key to shaping the large-scale features of intracranial enrichment patterns, with the potential to span a wide range of individual and cohort variability. Moreover, we predict that CSF production, cardiac- and respiratory pulsatility is not sufficient to explain early perivascular enrichment, but that fluid flow induced by low-frequency vasomotion in surface periarterial spaces (on the order of 10 μm/s) is sufficient, even in the absence of a structural compartmentalization of the PVS. Conversely, enlarged PVSs in the SAS will cause a substantial reduction in cardiac- and vasomotion-driven flow velocities, strongly delay perivascular transport, and thus impair intracranial enrichment. These findings transfer, reconcile, integrate and extend insights from clinical, experimental, and theoretical studies, and lay a new foundation for in-silico studies of personalized intrathecal drug delivery and brain clearance.

Results

In-silico predictions of intracranial molecular enrichment and clearance after intrathecal injection

Using previously published multi-modal magnetic resonance imaging (MRI) data^{66,69–72}, we construct a multiscale computational representation of the human intracranial compartments consisting of the CSF spaces and brain parenchyma as three-dimensional (3D) domains and with the PVSs surrounding major surface arteries and veins as embedded networks of topologically one-dimensional (1D) curves (Figure 1A–B). We consider a solute concentration field, varying in space and time, in the 3D domains and in the PVS networks, and assume that the solute can cross between these compartments through semi-permeable membranes. As the drivers and modes of intracranial transport are under substantial debate^{13,14,73–75}, our first target is to establish a baseline model accounting for a reasonably conservative set of mechanisms and their integrated effect over a timescale of several minutes to a few days. To this end, we assume that the solute will (i) diffuse within all compartments, with diffusivity depending on the effective properties of the relevant medium⁷⁶; (ii) experience significant dispersive effects due to the pulsatile flow of CSF induced by the cardiac and respiratory cycles^{43,46,55,77}; and (iii) be convected by a (small) net flow of CSF resulting from production in the choroid plexus with CSF efflux across the upper convexity⁷⁸ and from the peristaltic pumping effect of pulse wave pulsations in surface periarterial spaces^{33,40}. Mathematically, this model is represented by a mixed-dimensional system of coupled time-dependent partial differential equations⁶⁵, which we solve numerically with high accuracy using a mass-conserving finite element scheme and the FEniCS finite element software^{79,80} (see Methods). The computational framework and associated software are all openly available⁶⁸.

Simulating a glymphatic MRI protocol^{11,15,28} (Figure 1C), we then predict the spreading of 0.5 mmol intrathecally injected Gadobutrol after its appearance at the craniocervical junction (Figure 1D–E). After one hour, the in-silico tracer moves upwards in the SAS frontally of the brainstem, and quickly reaches the supratentorial regions. Here, it spreads both posterior through the quadrigeminal cistern and the longitudinal fissure, and anteriorly through the outer SAS, reaching the top of the cerebral cortex after around 12 hours. After 24 hours, the tracer covers most of the brain surface (with the exception of some posterior regions) and has penetrated substantially into the parenchymal tissue. This pattern is reflected in the mean tracer concentrations in each compartment, where the CSF space reaches its peak of 1.4 mmol/l after 2 hours, followed by the arterial PVS concentration peak (2.9 mmol/l after 4 hours) (Figure 1F). While the mean concentrations in these compartments drop soon after peaking, the parenchymal tissue slowly enriches with tracer over the first 24 hours, with a final value of 0.3 mmol/l. Overall, about 40% of the total amount of tracer remains in the cranium 24 hours post-injection, with the largest share in the CSF (53%), followed by the parenchyma (35%), the venous PVS (8%) and the arterial PVS (5%) (Figure 1G).

Reduced CSF pulsatility strongly shifts intracranial enrichment patterns

The enrichment patterns observed clinically after intrathecal injection of contrast differ substantially between subjects and between pathological conditions^{7,15–17}. These neurological conditions are also associated with alterations in the pulsatile flow of CSF in the ventricular system and SAS¹⁶. Clearly, key physiological factors such as cardiac pulsatility and respiration easily differ between individuals and between both pathological and physiological states. We therefore next asked to what extent – and how – variations in CSF pulsatility would affect the intracranial enrichment characteristics.

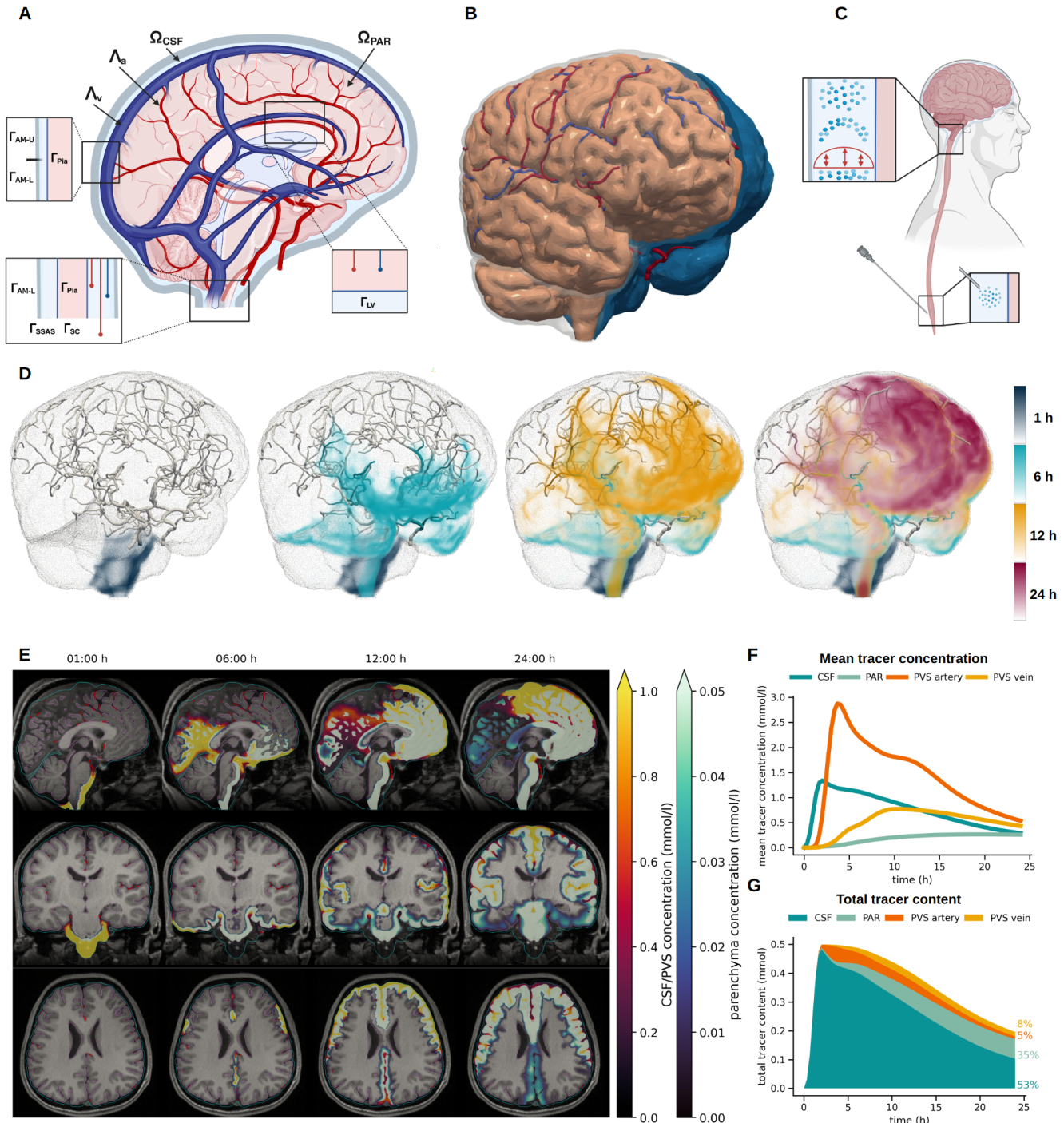


Figure 1. In-silico modelling of molecular enrichment and clearance of the PVS, SAS and parenchyma. A) Illustration of the model geometry including the CSF-filled spaces (ventricles and SAS) Ω_{CSF} , the parenchyma Ω_{PAR} and the PVS surrounding arteries Λ_{artery} and veins Λ_{vein} , as well as their interfaces and boundaries; B) 3D rendering of the computational geometry: the parenchyma, CSF (clipped, blue), arterial network (red), and venous network (blue); C) illustration of model representation of the intrathecal tracer injection; D) in-silico predictions of tracer concentration after 1, 6, 12, and 24 hours (opacity increasing linearly from 0 to 2 mmol/l); E) sagittal, coronal and axial view of in-silico tracer concentrations overlaid on T1-weighted MR image after 1, 6, 12 and 24 h (low concentrations transparent, pial surface in pink, arachnoid membrane in cyan, and arteries in dark red); F) average tracer concentration in each compartment over the first 24 h; G) total amount of tracer in each compartment over the first 24 h.

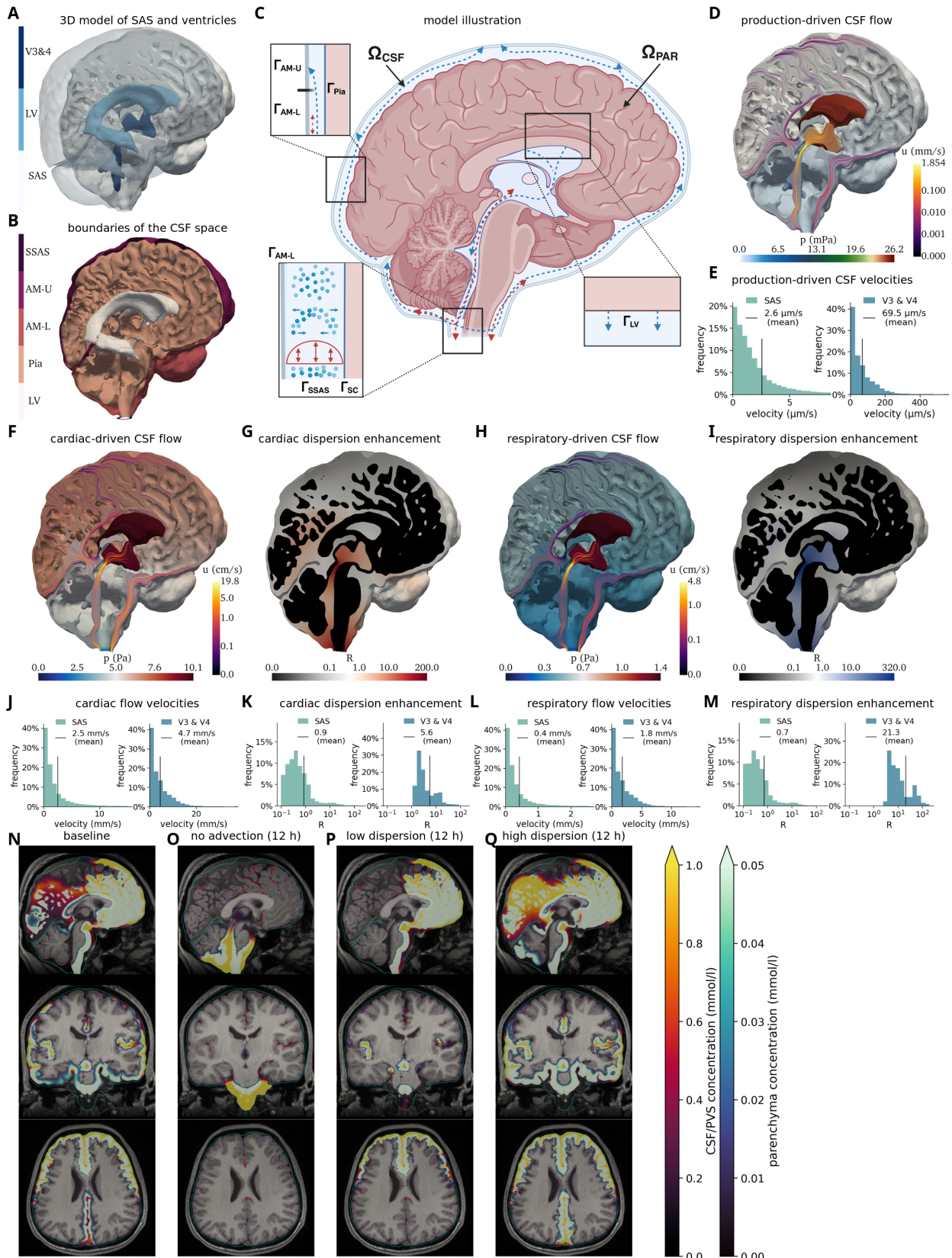


Figure 2. The balance between CSF pulsatility and production shapes molecular enrichment patterns. A) CSF spaces: the third and fourth ventricle (V3&4), lateral ventricles (LV) and SAS; B) Boundaries and interfaces: the spinal subarachnoid space (SSAS), upper and lower arachnoid membrane (AM-U and AM-L), pia (Pia) and lateral ventricles (LV); C) Schematic of the CSF flow model; D) CSF flow induced by CSF production with outflow allowed across the upper convexity (AM-U);

Figure 2. (cont.) E) Histograms of the production-induced CSF velocities in the SAS and third and fourth ventricle (V3 & V4) in terms of the relative frequency of the mean flow speed in each computational cell weighted by its volume; F) CSF flow induced at peak systolic blood inflow; G) Cardiac-induced dispersion factor R_c ; H) CSF flow induced at peak respiratory expansion; I) Respiration-induced dispersion factor R_r , $D = (1 + R_c + R_r)D^{\text{Gad}}$; J–M): Histograms of the cardiac-induced flow velocities (J), cardiac-induced dispersion factors (K), respiratory flow velocities (L), respiratory dispersion factor (M); N–Q): sagittal, coronal and axial planes of tracer concentration after 12h for different model variations: baseline (N), no CSF production (O), low dispersion (P), and high dispersion (Q).

For the CSF dynamics in our baseline model, we combine the net contribution to CSF flow induced by CSF production with the integrated dispersive effects of cardiac and respiratory pulsatile CSF flow (Figure 2A–C). Imposing a constant CSF production of 400 ml/day across the surface of the lateral ventricles, while allowing for efflux across the upper convexity, yields a total CSF pressure drop of 26 mPa (0.00020 mmHg) (Figure 2D) with a maximum flow velocity of 1.85 mm/s (in the aqueduct) and a mean velocity in the SAS of 2.6 μm/s (Figure 2E). To examine the dispersive effects of pulsatile CSF flow, we employ the theory of shear-augmented dispersion together with computational fluid dynamics to determine a dispersion factor R enhancing the effective solute diffusivity (see Methods). For the cardiac contribution, we compute CSF pressure and flow fields at peak systolic blood inflow, corresponding to a reduction in CSF space volume at a total rate of 6 ml/s^{56,81} in the SAS and 0.31 ml/s across the lateral ventricle surface⁵⁵. This scenario sets up a pressure drop of 10 Pa (0.075 mmHg) between the lateral ventricles and the spinal SAS and a maximum flow velocity of 19.8 cm/s (Figure 2F, J). Assuming a cardiac frequency of 1 Hz, we infer that this cardiac-induced pulsatile CSF flow increases the effective diffusion by more than two orders of magnitude in the aqueduct and near the cisterna magna, but has little effect ($R < 1$) in most of the SAS (Figure 2G, K). For the respiratory contribution, we employ the same methodology, but with a total rate of 1 ml/s⁸² in the SAS and 0.121 ml/s⁸³ in the lateral ventricles, yielding a respiratory peak flow volume of 1.121 ml/s at the craniocervical junction. While the resulting flow velocities are only about one fourth of their cardiac-induced counterparts (Figure 2H, L), respiratory dispersive mixing reaches a factor of up to 320 due to the lower respiratory frequency of 0.25 Hz (Figure 2I, M).

Now, to examine how CSF pulsatility affects the enrichment patterns, we consider three variations of the baseline: (i) no CSF production, (ii) reduced pulsatility and thus decreased dispersion ($0.1 \times R$), and (iii) higher pulsatility with increased dispersion ($10 \times R$). Without CSF production, transport is considerably delayed (Figure 2N, O). Even after 12 hours, tracer remains in the subtentorial regions around the cerebellum, the brain stem and in the surrounding CSF. Interestingly, the lack of CSF production instead allows tracer to travel upwards through the ventricular system, reaching the third ventricle after around 12 hours. On the other hand, if the CSF pulsatility is reduced, we observe rapid transport towards the upper convexity of the cranium, as in the baseline model, but the tracer spreads exclusively within the anterior regions (Figure 2P). This feature can be attributed to the CSF flow bifurcation posterior to the ambient cistern (Figure 2D): without sufficient diffusion, the tracer is unable to cross into the posterior SAS. Indeed, with higher dispersion, the tracer moves through the quadrigeminal cistern and further upwards into the longitudinal fissure, with also enrichment of the cerebellum (Figure 2Q).

Perivascular flow shapes and accelerates molecular enrichment

The PVSs are recognized across species as critical pathways for solute transport in and around the brain, and thus as potential targets for enhancing brain drug delivery and metabolic waste clearance. However, whether CSF flows more rapidly in PVSs and what the forces and mechanisms required to drive such flow are, remain as key points of debate^{14,27}. Motivated by experimental observations in animal models^{10,31–33}, there is now a remarkable body of literature on modelling perivascular fluid flow and transport^{36–47}. Here, we ask how these proposed mechanisms would translate from idealized geometries to human vascular networks and moreover, evaluate their integrated effect in the context of intracranial solute transport.

Our periarterial network extends from the internal carotid arteries and basilar artery through up to 18 bifurcations to reach upstream network ends located within the SAS or up to 6 mm inside the parenchyma (Figure 1A–B, Figure 3A) and includes major surface arteries of radius 0.5–1.4 mm. Imposing the pressure field induced by CSF production at the periarterial network ends induces slow steady CSF flow of variable direction in these PVSs, with an average velocity of 0.08 μm/s (antegrade) and a maximum velocity of 0.55 μm/s (Figure 3B). On the other hand, traveling waves of arterial wall motion (Figure 3C), such as the pulse wave or other vasomotion^{9,84–87}, also induce net directional flow in the PVS^{39–41,45,88} – of magnitude and direction depending on the amplitude, frequency, and length of the waves and the characteristics of the perivascular network⁴⁰. Applying a semi-analytic model of the net flow induced by peristalsis in perivascular networks⁴⁰ (see Methods), we estimate that the cardiac pulse wave alone, traveling at a frequency of 1 Hz with a wavelength of 2.0 m and a 1% wall displacement⁸⁹, will induce mainly antegrade PVS flow with an average net velocity of 0.92 μm/s while reaching up to 7.31 μm/s near larger, ventral vessels such as the MCA (Figure 3D,E). The same theory predicts that strong ultraslow vasomotions, if traveling antegrade at 0.1Hz with a wavelength of 0.02 m and a 10% displacement⁸⁷, will induce both retrograde and antegrade net PVS flow with an

133 average velocity of 13.05 $\mu\text{m/s}$ and maximum velocity 54.44 $\mu\text{m/s}$ (Figure 3D,F).

134 We study the effect of such rapid PVS flow on intracranial molecular enrichment by comparing the more conservative
135 baseline model and a high PVS flow model, where the former still includes the net flow contributions from CSF production and
136 the cardiac pulse wave, while the latter additionally includes the ultraslow vasomotion contribution. In both models, tracers
137 were first observed at the basal artery after 48 minutes (Figure 4A), defined by their first-time arrival (FTA), the time at which
138 the concentration first exceeds 0.1 mmol/l. At all upstream locations along the middle cerebral arteries (MCAs) and anterior
139 cerebral artery (ACA), we found substantially reduced FTAs with higher PVS flow (Figure 4B), up to 2.5 hours earlier in the
140 left M2 segment of the MCA. PVS concentrations peaked before the surrounding tissue (0:48h vs 1:12h at the MCA and 1:00h
141 vs 1:48h at MCA2) with high PVS flow, while these peaks occurred nearly simultaneously in the baseline model. The earlier
142 appearance and the delay in time-to-peak between the PVS and surrounding tissue clearly indicates the directionality of tracer
143 enrichment – it first arrives in the PVS and subsequently spreads into the tissue and SAS (Figure 4C, D), and especially so with
144 higher PVS flow. These observations also hold on an aggregated level: computing the total amount of tracer in the PVS as
145 a function of the distance to the arterial network roots, we find accelerated tracer transport with higher PVS flow, especially
146 at earlier time points (2–9 hours) (Figure 4E). Moreover, differences in tracer transport along the PVS translate to altered
147 enrichment patterns on the whole-organ scale. For instance, after 4–6 hours, the faster-moving tracer in the PVS is clearly
148 visible in the space adjacent to the PVS of the ACA, MCA, and other arteries (Figure 4G). In contrast, there are no clear signs
149 of early enrichment surrounding the PVS in the baseline model (Figure 4F).

150 A natural question is whether early PVS enrichment could be the result of increased dispersion rather than net flow in the
151 PVS^{42, 42, 43, 46, 86}. Interestingly, even increasing the dispersion factor by 100× in the PVS, induced only minor changes in the
152 global spreading rate compared to the baseline (Figure 4F, H), thus indicating a negative answer to this question.

153 **Structural versus functional compartmentalization of perivascular spaces**

154 Human and rodent observations indicate that tracers concentrate in perivascular spaces surrounding the pial and subarachnoid
155 vasculature^{22, 28, 32, 33, 60, 90}. However, it remains unclear whether such enrichment patterns necessitate a structural barrier, such
156 as a membrane with limited permeability, or if the patterns could result from enhanced flow or mixing in these areas alone.
157 We therefore next investigate how the permeability of the interface between the PVS and the surrounding CSF affects tracer
158 enrichment around the major arterial trunks (Figure 5A–B). To this end, we compare models with high and low permeabilities,
159 representing a highly permeable PVS-CSF interface (functional compartmentalization) and a less permeable interface (structural
160 compartmentalization), respectively. For the low permeability model, we set the permeability to $3.8 \cdot 10^{-7} \text{ m/s}$, consistent with
161 previous estimates for the endfoot sheath surrounding penetrating arterioles⁹¹, which we consider to be a lower bound for the
162 surface PVS-CSF permeability. For the high permeability model, we increase this permeability by a factor of 100. For both
163 scenarios, we consider the high PVS flow regime as examined in the previous section.

164 At the basal artery (BA), tracer appears within one hour in the surrounding CSF in both models (Figure 5C, E). With a more
165 permeable PVS-CSF interface, tracer quickly crosses from the CSF into the PVS, resulting in similar peak concentrations of
166 25 mmol/l in the PVS and at its outer surface, while values up to 50 mmol/l are attained in the vicinity. In contrast, the low
167 permeability model exhibits substantially lower perivascular tracer enrichment, with a maximum concentration of 10 mmol/l
168 after approximately two hours. For the middle cerebral arteries (MCA-R and MCA-L), tracer appears first in the PVS in both
169 models (Figure 5D, E), though with higher concentrations in the high permeability model (up to 24 mmol/l). We also observe
170 that the higher permeability allows the tracer to leak out of the PVS and spread within the Sylvian fissure to a greater extent.
171 With a small delay, more tracer appears via the CSF pathway (Figure 5D). At the anterior cerebral artery (ACA-A2), the first
172 tracer arrival in the PVS occurs after 3 hours, with a peak at 5 hours. The concentration peak in the PVS is tailed by a higher
173 peak in the CSF (Figure 5E), indicating tracer arrival through a second pathway; i.e., directly through the CSF-filled space
174 outside of the PVS. Similar patterns are observed for ACA-A3.

175 Summarizing and quantifying these observations (Figure 5F), we find that neither the time of first arrival nor the time-to-peak
176 are substantially affected by the PVS-CSF permeability at any of the periarterial segments considered (BA, MCAs, ACAs).
177 However, the concentration difference between the PVS and its surrounding CSF quickly decreases with higher permeability,
178 as does the time lag between the concentration peaks in these domains. Thus, fast transport along the PVS is not contingent
179 upon a structural compartmentalization of the PVS, whereas a sharp concentration gradient between PVS and CSF is unlikely
180 without a restricting barrier.

181 **Enlarged PVSs delay periarterial and intracranial molecular enrichment**

182 Enlarged PVSs are associated with impaired periarterial tracer transport and more generally with cognitive decline as well
183 as certain subtypes of dementia^{28, 92}. A key question is thus whether enlarged PVSs alone leads to delayed perivascular and
184 intracranial tracer enrichment. To address this question from a fluid and transport dynamics perspective, we ask our in-silico
185 model to predict the integrated effect of perivascular dilation on PVS flow velocities and tracer enrichment patterns (Figure 6A).

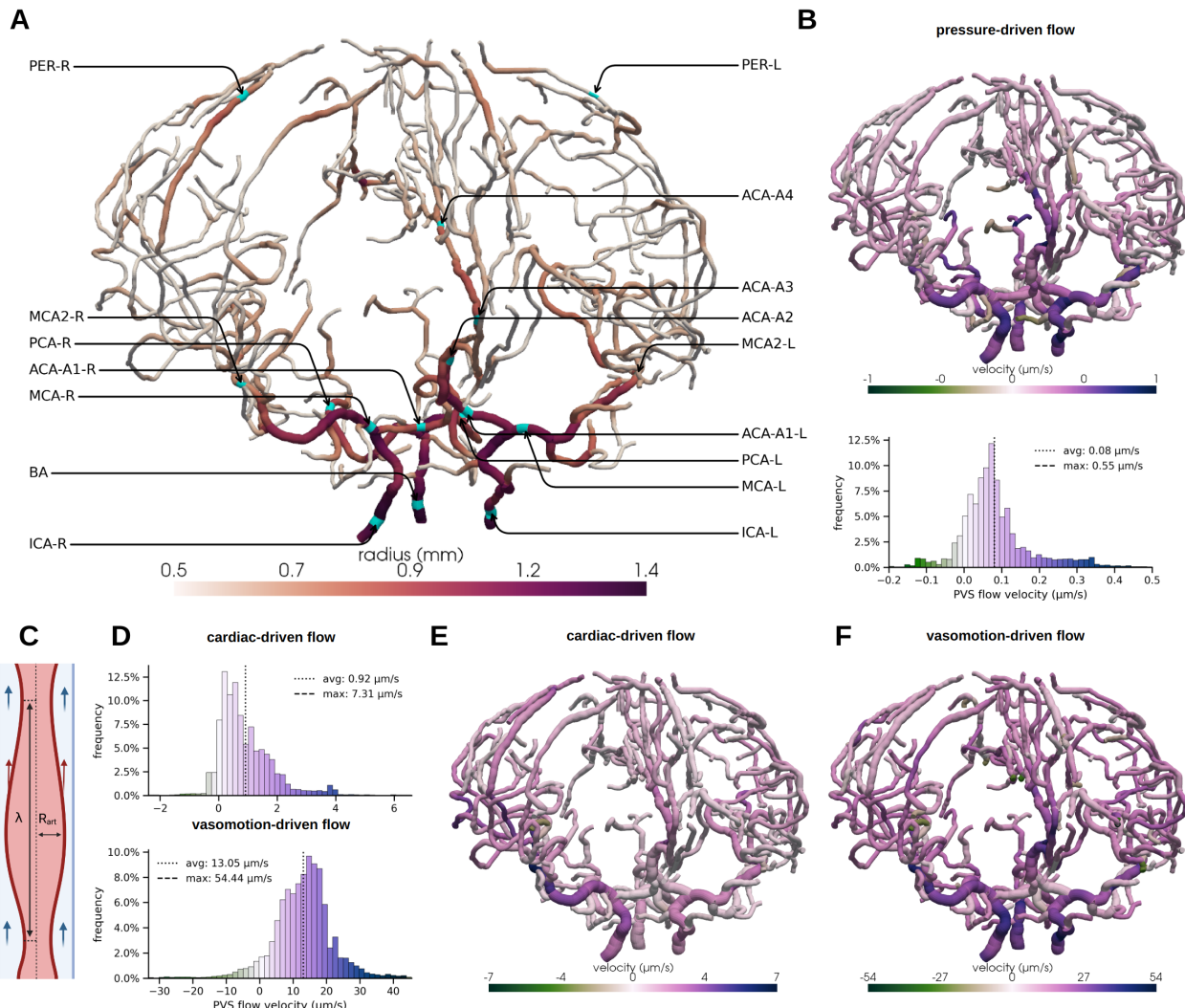


Figure 3. A static pressure gradient and peristaltic pumping are potential drivers of perivascular flow. A) Surface arterial network colored by arterial radius with vessel locations labeled; B) Net PVS flow induced by CSF production (cf. Figure 2 – histograms show the relative frequencies of local periarterial velocities. Positive values indicate antegrade PVS flow, while negative values indicate retrograde PVS flow; C) Illustration of the concept of peristaltic pumping; D) histograms of estimated net PVS flow induced by pulse wave or vasomotion peristaltic pumping; E) Estimated net PVS flow induced by pulse wave peristaltic pumping. F) Estimated net PVS flow induced by vasomotion/slow wave peristaltic pumping.

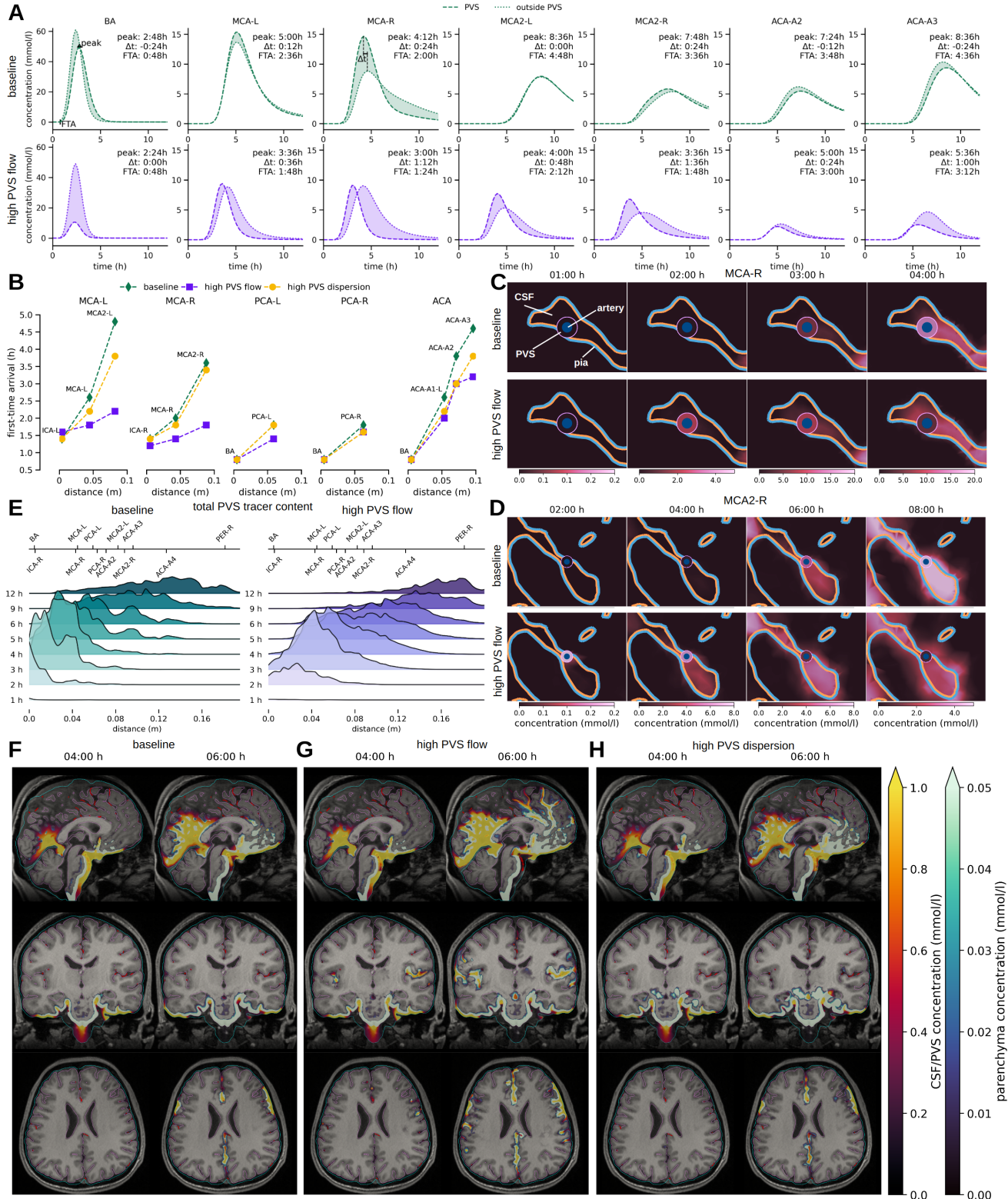


Figure 4. Perivascular flow shapes and accelerates molecular enrichment. A) Comparison of mean tracer concentration in the PVS and over the outer PVS surface at key locations of the arterial tree, for the baseline (lower) and high PVS flow (upper) models, with labels: “peak”: time-to-peak (h), “ Δt ”: time difference between peaks (h), and “FTA”: first-time tracer arrival (h). B) first-time arrival for the main trunks of the periarterial network over the distance from the closest network root node (BA, ICA-R or ICA-L for the baseline, the high PVS flow and the high PVS dispersion models);

Figure 4. (cont.) C, D) 2D slices showing zoom-in on the region surrounding the MCA-R and MCA2-R for the baseline (upper) and high PVS flow (lower) models. Innermost circle indicates the artery (blue), the surrounding annulus is the PVS (color represents concentration value), the surroundings are parenchyma and/or CSF spaces, separated by the pia (blue: towards the parenchyma, pink: towards the CSF); E) Total amount of tracer in the periarterial spaces as a function of the distance to the nearest network root over time for the baseline (left) and the high PVS flow (right) models; F–H) sagittal (upper) and coronal (lower) views of the simulated tracer concentrations overlayed on the T1-weighted MR image after 4 and 6h for the baseline (K), high PVS flow (L) and high PVS dispersion (M) models (concentration opacity linearly increasing with concentration value, pial surface outlined in pink, arachnoid membrane in cyan, and arteries in dark red). An interactive visualization of the baseline and the high PVS flow model can be found [here](#), and [here](#).

Again we compute CSF production-, cardiac-, and vasomotion-induced net PVS flow velocities, but now in a perivascular geometry with an increased outer radius ($R_2^{\text{dilated}} = 3R_1$) compared to the previous ($R_2^{\text{control}} = 2R_1$), which corresponds to a $2.67 \times$ increase in PVS cross-section area. The enlargement yields notable and non-uniform changes in the flow dynamics. On the one hand, the pressure-induced flow velocities increase from a mean of $0.08 \mu\text{m/s}$ to $0.33 \mu\text{m/s}$ due to the reduced effective resistance of the PVS. However, the peristaltic pumping becomes considerably less effective: the cardiac and vasomotion-induced net CSF flow velocities drop from a mean of $0.92 \mu\text{m/s}$ to $0.17 \mu\text{m/s}$ and from $13.05 \mu\text{m/s}$ to $2.33 \mu\text{m/s}$, respectively (Figure 6B–D). In total, the net CSF velocity reduces, which in turn alters the tracer enrichment within the dilated PVS. Notably, we observe later tracer arrival in all MCA segments, with up to 96 min later arrival in the MCA2s for the high PVS flow scenario (Figure 6E, F). For the baseline model, which omits the vasomotion-induced net PVS flow, the effect is less pronounced in the MCA but clearly persists and is evident in the MCA2s (Figure 6F). Finally, we note that the larger volume of the dilated PVS results in a greater total accumulation of tracer in the PVS from 3–24 hours and reduced enrichment of the parenchyma at 6 and 12 h, while the mean PVS concentration is initially lower, but later exceeds the baseline model (Figure 6G,H).

Discussion

We have presented a high-fidelity in-silico model of molecular enrichment and clearance in human intracranial spaces, enabling tailored predictions of the influence of CSF space and (peri)vascular morphology, physiological factors such as cardiac and respiratory pulsatility, as well as of pathological conditions such as enlarged PVSs. A key observation is that the balance between CSF production and intracranial pulsatility significantly shapes the large-scale features of molecular enrichment, with e.g. ventricular tracer reflux after intrathecal injection in the absence of CSF production, and preference towards anterior brain regions with reduced pulsatility. Indeed, the simulated distribution patterns cover a substantial range of the individual variations observed clinically¹⁵. In terms of perivascular pathways, we find that even moderate CSF flow on the order of $0.1\text{--}1.0 \mu\text{m/s}$ in the surface PVSs results in earlier tracer enrichment around major cerebral arteries. This effect is more pronounced – with up to a three-hour difference in time of arrival – with mean PVS flow rates of approximately $10 \mu\text{m/s}$. Our models of CSF flow in perivascular networks, based on first principles and asymptotic analysis, predict net flow of such magnitudes and both antegrade and retrograde flow within the perivascular network, occurring with or without pressure differences at the network ends. The PVS may thus function as highways facilitating rapid transport, even in the absence of structural barriers, though a sharp concentration difference between the PVS and surrounding tissues is unlikely without such barriers. Finally, dilated PVS will cause a substantial reduction in cardiac- and vasomotion-driven flow velocities, which in turn impedes perivascular transport.

While molecular enrichment of the brain and surrounding CSF spaces have been extensively studied in animal models, especially in murine models in connection with studies of the glymphatic system, there are fewer reports of contrast enrichment in human subjects over 0–24h. We therefore mainly compare our in-silico predictions with the series of papers by Eide and colleagues^{6,11,15,28} and Watts et al⁶⁷. Ringstad et al.¹⁵ report of tracer enrichment in a centripetal pattern, primarily in regions near large cerebral surface arteries, peaking in the CSF spaces between 6 and 9 hours, with parenchymal tracer content still increasing after 24 hours, but with large individual differences. Watts et al⁶⁷ report of a similar enrichment pattern and a concentration peak in the SAS of $\approx 0.5 \text{ mmol/l}$ (relative to a total amount of 1.0 mmol) occurring after 10 to 15 hours. Our in-silico enrichment patterns agree with these observations, though with an earlier rather than later peak in the CSF spaces (2 hours after first tracer appearance at the craniocervical junction). In particular, we note that the substantial individual variation observed clinically is comparable to the variation in in-silico enrichment patterns associated with reduced CSF production or reduced intracranial pulsatility. We find that about 20% of the tracer reaching the cranium enters the parenchyma, which aligns with the reported peak concentration values of 0.5 mmol/l in the SAS and 0.1 mmol/l in the parenchyma reported by Watts et al⁶⁷. In terms of perivascular tracer enrichment, Eide and Ringstad²⁸ report of first-time tracer appearance in the PVS of the MCA after 37.8 ± 47.0 (M1), 53.1 ± 50.5 (M2) and 82.6 ± 61.5 (M3) min after injection, thus with just a 15.3

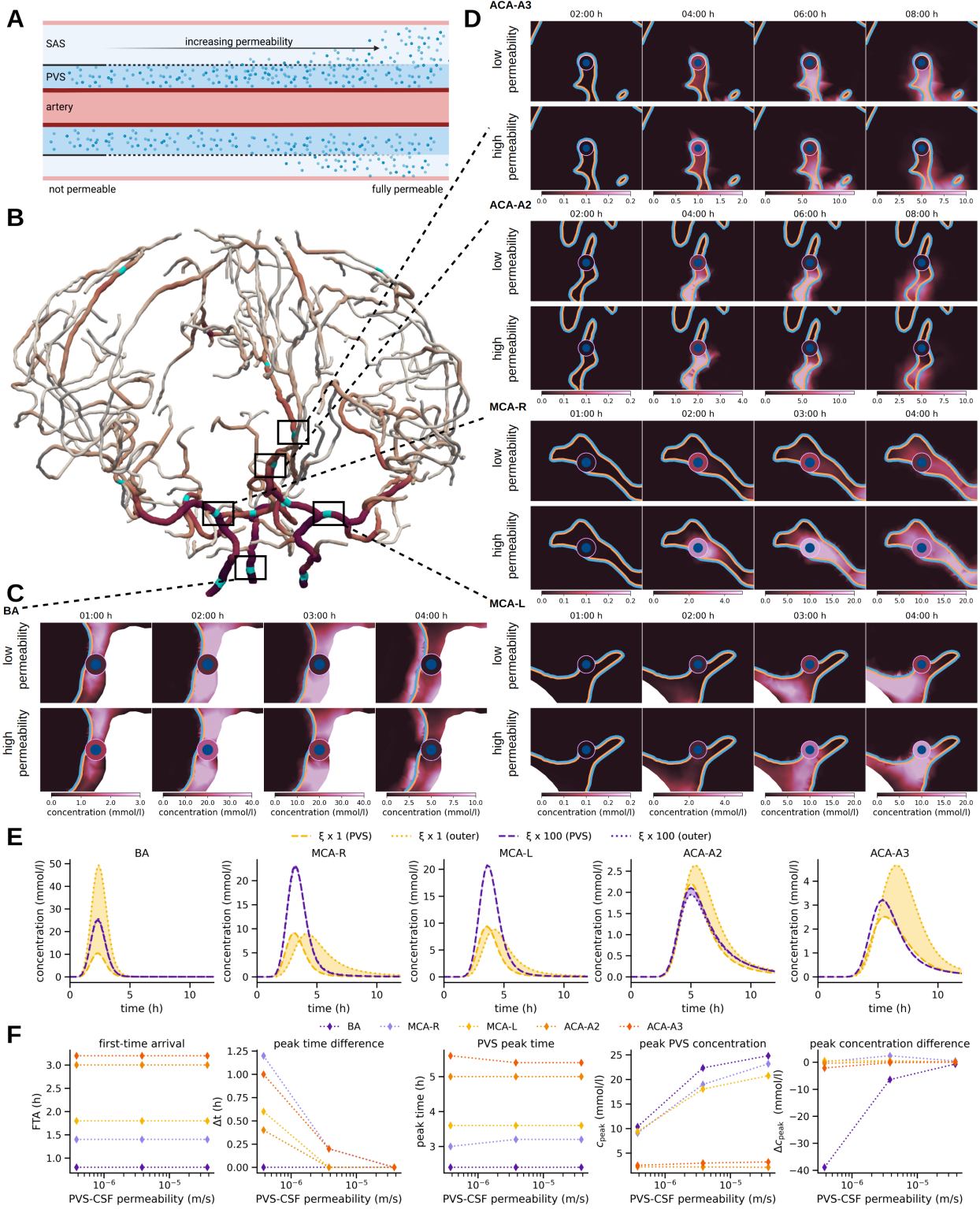


Figure 5. Does early perivascular enrichment rely on a structural compartmentalization of the PVS? A) The PVS-CSF membrane permeability regulates the exchange of solutes between the PVS and surrounding CSF spaces; B) The arterial network with highlighted regions of interest; C) 2D slices showing zoom-in to the region surrounding the basal artery after 1, 2, 3, and 4 hours for a low (above) and high (below) PVS-CSF permeability model. Innermost circle indicates the artery (blue), the surrounding annulus is the PVS (color represents concentration value), the surroundings are parenchyma and/or CSF spaces, separated by the pia (blue: towards the parenchyma, pink: towards the CSF)); D) As in (C) for regions surrounding (from upper to lower) the ACA-A3, ACA-A2, MCA-R and MCA-L segments;

Figure 5. (cont.) E) Comparison of mean tracer concentration in the PVS (dashed) and over the outer PVS surface (dotted) for the BA, MCA-R, MCA-L, ACA-2, and ACA3 segments over time for the high (purple) and low permeability (yellow) models; F) Effect of varying the PVS-CSF permeability on first-time-of-arrival (FTA), time difference (Δt) between concentration peaks in the PVS and surrounding tissue, time of PVS peak concentration, PVS peak concentration and difference in peak concentration between PVS and surrounding tissue.

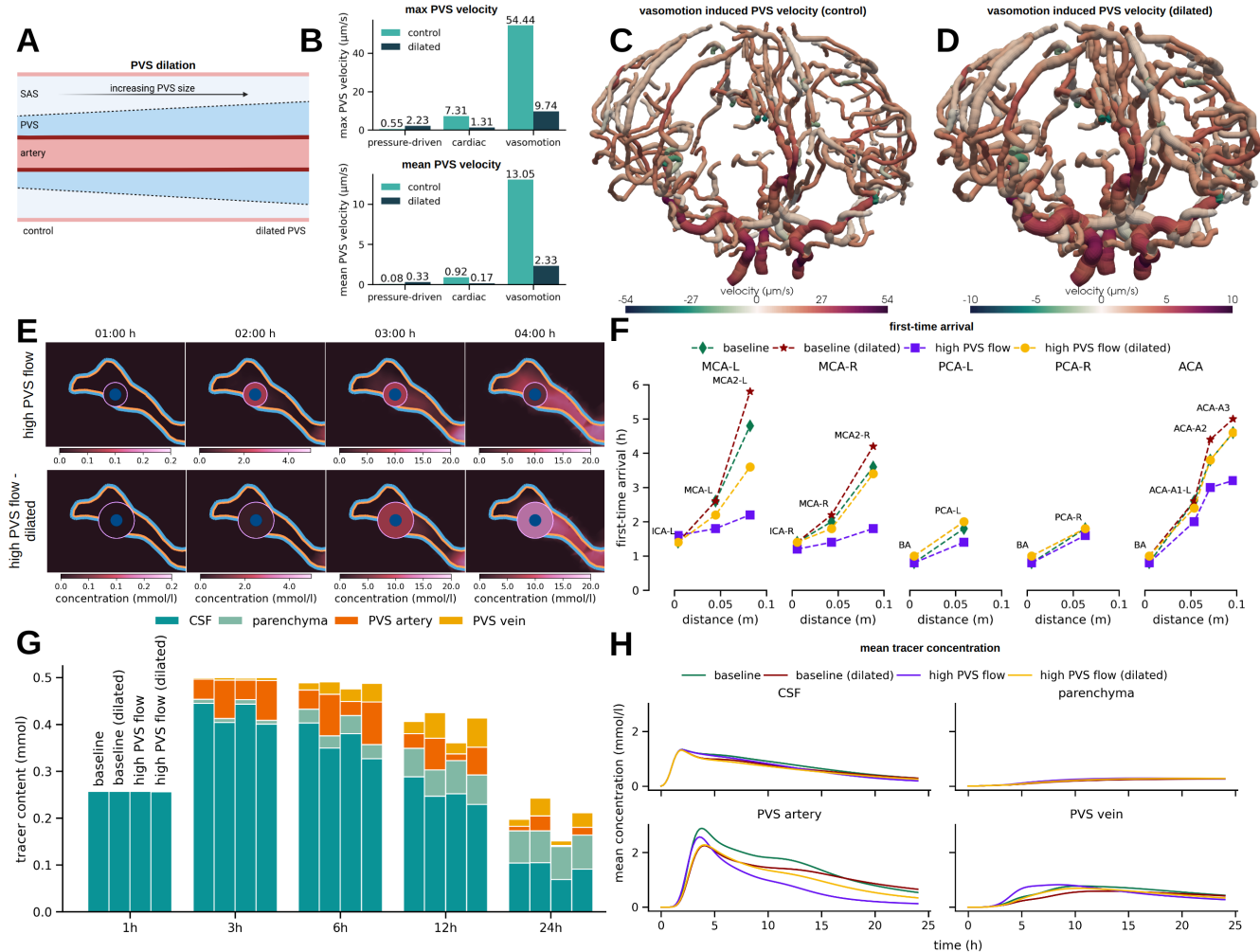


Figure 6. PVS enlargement reduces net PVS flow and delays tracer transport A) Modelling dilated PVS by extending the outer PVS boundaries; B) mean and max PVS flow velocities with normal/control and dilated PVS; C–D) 3D rendering of vasomotion-induced PVS flow in the normal (C) and dilated (D) periarterial networks; E) 2D slices showing zoom-in to the region surrounding the MCA-R after 1, 2, 3, and 4 h with normal (lower) and dilated (upper) PVS. Innermost circle indicates the artery (blue), the surrounding annulus is the PVS (color represents concentration value), the surroundings are parenchyma and/or CSF spaces, separated by the pia (blue: towards the parenchyma, pink: towards the CSF)); F) First-time arrival for different branches of the arterial tree for the baseline model (with pressure-driven and cardiac-induced net PVS flow) and the high PVS flow model (also including vasomotion-induced net PVS flow) for normal and dilated PVS; G) total tracer content in the CSF, parenchyma and arterial and venous PVS at 1,3,6,12 and 24 h for the four models from F; H) mean concentration in the CSF, parenchyma and arterial and venous PVS over time for the four models from F.

228 min delay between M2 and M1. Comparing with our FTAs in the MCA segments, we note that the baseline model predicts a
229 more-than 3 hour difference in FTA between the M1 and M2. In contrast, the high PVS flow scenario predicts a 24 min delay
230 between these segments. Moreover, the high PVS flow scenario predicts FTAs of 84–108 min (M1) and 108–132 min (M2) after
231 tracer appearance at the craniocervical junction. Assuming a tracer travel time from the point of injection to the craniocervical
232 junction of 13 min (as reported by Eide and Ringstad²⁸), our predictions fall at the upper end of the clinical ranges. This can
233 partly be attributed to the limited caudal extend of our PVS network, with the lowest point located approximately 4 cm above
234 the craniocervical junction due to imaging constrains. We interpret these results as indicative of a net CSF flow in human
235 surface PVS beyond what would be induced by CSF production and cardiac peristalsis alone.

236 The existence, magnitude, and directionality of flow in surface and parenchymal PVSs have been the subject of active
237 debate for decades^{10, 14, 21, 24, 30–34, 36–41, 44, 47, 84, 93}. In mice, Mestre et al³³ observe CSF flow in surface perivascular regions
238 surrounding branches of the MCA with average flow speeds of 18.7 $\mu\text{m/s}$ and net flow in the antegrade direction, but also
239 regions with retrograde flow. Similarly, Bedussi et al.³² report of oscillatory flow, with an average (net) CSF velocity of 17 ± 2
240 $\mu\text{m/s}$ in the antegrade direction. Using physics-informed neural networks, Boster et al³⁴ estimate PVS velocities of 12.75 ± 6.25
241 $\mu\text{m/s}$. Less is known about the magnitude and directionality of CSF flow in surface PVSs in humans. Here, assuming that
242 human surface PVS follow the major surface vessels and are CSF-filled but otherwise open regions of width proportional to
243 the vessel radius, our estimates indicate that the CSF pressure differences due to CSF production, cardiac peristaltic pumping
244 and low-frequency vasomotion all yield spatially-varying net CSF flow with both antegrade and retrograde PVS segments.
245 This observation is thus in agreement with the experimental observations^{32, 33}, and inherently supports the original notion
246 that antegrade and retrograde solute transport along PVSs may coexist²¹. In terms of magnitude, the contribution from CSF
247 production and cardiac wall motion are small ($0.08 \mu\text{m/s}$ and $0.92 \mu\text{m/s}$ on average), but intriguingly, our estimates of the
248 contribution from vasomotion ($13.05 \mu\text{m/s}$) are comparable to the experimental reports. We do note that this estimate is based
249 on the presence of rhythmic waves of vasomotion at a frequency of 0.1Hz, a wavelength of 20 mm, and a wall displacement of
250 10% – in the antegrade direction, all values currently associated with significant uncertainty^{84, 87, 94}.

251 To what extent are surface PVSs in communication with the surrounding SAS and to what extent are these structurally
252 separated compartments? Originally, Weller and coauthors^{22, 59, 90} identified thin sheaths of pial cells surrounding human
253 surface arteries and penetrating arterioles (but not veins or venules). On the other hand, Bakker and coauthors report that
254 the subarachnoid space, the cisterns, ventricles and penetrating periarteriolar spaces form a continuous CSF space⁶⁰. Thorne
255 and colleagues study the architectures of rat perivascular spaces in detail, emphasizing the presence of openings (stomata) on
256 the interface between the vasculature and the CSF within the SAS^{26, 61}. Further, Mestre et al⁶² study the properties of pial
257 perivascular spaces in mice, and report of pial cells forming sheaths for larger surface arteries and partially cover smaller
258 surface arteries, with higher coverage in ventral SAS regions. Our results demonstrate that the PVSs may act as rapid transport
259 pathways even with only a partial barrier between the PVS and surrounding CSF, thus contributing to quantifying the properties
260 of the human PVS-CSF interface²⁸.

261 Lifestyle factors such as sleep^{5, 6, 8, 9, 86, 95, 96}, exercise^{97, 98}, and alcohol intake⁹⁹ affect molecular enrichment and clearance
262 of the brain. In particular, pial arteries display higher-amplitude low-frequency vasomotion during NREM and intermediate
263 sleep states, while REM sleep is associated with reduced PVS width⁸⁶. Peristaltic pumping is more effective under both of
264 these configurations, resulting in higher estimated net PVS flow velocities⁴⁰. Even higher PVS velocities would amplify the
265 PVS flow effects simulated here, with earlier arrival times along the PVSs, clear enrichment in adjacent spaces, and accelerated
266 molecular enrichment overall. Moreover, sleep is linked with low-frequency oscillations in human CSF flow⁵⁴. As we have
267 shown here, the level of dispersion in the CSF spaces strongly shapes molecular enrichment patterns. While we, at baseline,
268 account for the dispersion induced by cardiac and respiratory pulsatility, the high dispersion scenarios considered can be viewed
269 as representative of additional pulsatility induced by e.g. neural waves^{54, 57} or other respiration patterns depending on activity
270 level. More broadly, we consider this as a key strength of the current in-silico framework: allowing for integrating and exploring
271 the mechanistic macroscale implications of changes in pulsatility at smaller spatial or temporal scales.

272 In terms of limitations, our primary constraint modelling-wise is the geometric representation of the vascular (and therefore
273 also perivascular) networks. Concretely, we account for no vessels below the original MRI resolution limits, and thus only a
274 part of the cerebral surface vasculature and effectively not the cortical vessels. In addition, and again due to lack of resolution,
275 there is uncertainty associated with the location of the vessel segments relative to the CSF spaces and parenchyma, with some
276 vessels surrounded by both domains and some vessels completely entering the parenchyma before returning to the SAS. Higher
277 resolution MRI data (T1w and e.g. time-of-flight, QSM or other modalities) in more subjects would immediately allow for more
278 detailed studies of this aspect. As a result of the lack of an accurate representation of the cortical and subcortical white matter
279 vasculature, we have considered a conservative transport model within the parenchyma, modelling extracellular diffusion alone.
280 To compensate, we have focused on reporting detailed predictions in the CSF spaces and surface PVS after not more than 24
281 hours. In particular, we note that, we observe tracer accumulation at the perivascular network ends after 12 hours, similar to that
282 previously observed for microspheres^{32, 33}, which here can be interpreted as an artifact of the incomplete network creating up a

barrier for tracer movement. Previously, we have found that enrichment within the parenchyma is well-represented by $\approx 3\times$ enhanced diffusion augmented by local clearance e.g. across the blood-brain barrier or diffusion-convection with a complex pattern of spatially-varying convective velocities of 1–10 $\mu\text{m}/\text{min}$ ⁹⁵. We will incorporate such transport mechanisms within the parenchyma in future work. Finally, we also note that we simulate the intracranial distribution of a tracer concentration appearing at the craniocervical junction rather than as an intrathecal injection. We therefore overestimate the amount of tracer entering into the intracranial spaces; however, due to the linearity of the mathematical model, it is valid to directly interpret the in-silico concentrations relative to the total amount of tracer.

In conclusion, our findings transfer insights from experimental studies and theoretical analysis to the in-silico human setting, reconcile seemingly conflicting observations in particular relating to directionality of perivascular flow, and integrate different physical mechanisms across across spatial and temporal scales. The complete simulation pipeline is openly available, including interactive visualization of simulation results for all model variations⁶⁸. Looking ahead, this platform establishes a foundation for in-silico studies of molecular movement within the human brain environment, such as tailored predictions of intrathecal chemotherapy delivery or personalized diagnostics of brain clearance capacity.

Methods

Intracranial compartments: ventricular system, SAS, and brain parenchyma

From T1-weighted MR images of a 26-year-old, healthy male volunteer⁶⁶, we first automatically segment the brain parenchyma and CSF spaces, including the ventricular system and SAS, using Synthseg^{100,101} (Figure 1A–B). We next manually adjust the segmentation to accurately represent the connections and barriers between CSF spaces (aqueduct, median aperture, tentorium cerebelli), smoothen, and finally extract surface representations of the outer (arachnoid) boundary, the pial membrane and other interfaces. Conforming to these surface and interface representations, we generate a tetrahedral mesh Ω representing the complete intracranial volume as the union of the parenchyma Ω_{PAR} and CSF spaces Ω_{CSF} , using fTetWild¹⁰² (Figure 2A–B). The resulting computational mesh consists of 233 592 vertices and 1 290 131 mesh cells, which vary between 0.22 mm and 8.9 mm in mesh cell diameter. The parenchyma has a total volume of 1318 ml, whereas the ventricles and the outer SAS contribute 32 ml and 329 ml, respectively, to a total CSF volume of 361 ml, in agreement with recent estimates¹⁰³.

Periarterial and perivenous spaces

To represent surface networks of periarterial and perivenous spaces, we use Kiminaro¹⁰⁴ to separately skeletonize time-of-flight angiography (ToF) and quantitative susceptibility mapping (QSM) images from the same human subject⁶⁶. This technique yields networks of one-dimensional curves, each curve Λ^i indicating the centerline of a blood vessel segment and labeled with its lumen radius R_1^i (Figure 3A). We also assign an outer radius $R_2^i > R_1^i$ to each segment i , form the annular cylinder ensheathing Λ^i and define the union of these as the PVS. The periarterial network graph consists of 12 708 edges connected at 12 562 inner nodes and with 147 end nodes, and the associated domain is denoted by Λ_a . We identify three of the end nodes – corresponding to the two internal carotid arteries (ICAs) and the basilar artery (BA) – as root nodes, and designate the other ends as leaf nodes. The resulting perivenous network graph consists of 24 829 edges connected at 23 881 inner nodes and with 949 end nodes, and the associated domain is denoted by Λ_v . Finally, we label the outer surface of the PVSs associated with Λ_a and Λ_v , by Γ_a and Γ_v respectively.

Molecular transport equations

We model diffusion, convection, and exchange of a molecular solute in the PVS networks Λ_a and Λ_v , in the CSF spaces Ω_{CSF} and in the brain parenchyma Ω_{PAR} via a mixed-dimensional transport model^{65,105} over a timescale of minutes to hours (Figure 1A–B, Figure 2A–C). Specifically, for $t > 0$, we solve for a concentration $c = c(x, t)$ in the 3D intracranial compartments ($x \in \Omega_{\text{CSF}}, x \in \Omega_{\text{PAR}}$) and for a cross-section averaged concentration $\hat{c} = \hat{c}(s, t)$ in the periarterial and perivenous networks ($s \in \Lambda_a, s \in \Lambda_v$) such that the following equations hold:

$$\partial_t(\phi c) - \nabla \cdot (D \nabla(\phi c)) + \nabla \cdot (\mathbf{u} c) + \xi(\bar{c} - \hat{c})\delta_\Gamma = 0 \quad \text{in } \Omega_{\text{CSF}}, \Omega_{\text{PAR}}, \quad (1a)$$

$$\partial_t(A\hat{c}) - \partial_s(\hat{D} A \partial_s(\hat{c})) + \partial_s(A\hat{u}\hat{c}) + \xi P(\hat{c} - \bar{c}) = 0 \quad \text{in } \Lambda_a, \Lambda_v. \quad (1b)$$

In (1), $0 < \phi \leq 1$ is the fluid volume fraction, D and \hat{D} are effective diffusion coefficients, and \mathbf{u} and $\hat{\mathbf{u}}$ are fluid (CSF/ISF) velocities, all defined in the respective compartments; $P = 2\pi R_2$ is the perimeter and $A = \pi(R_2^2 - R_1^2)$ the area of the PVS cross-sections, δ_Γ is a Dirac term concentrated on the interfaces Γ_a, Γ_v , the overlined \bar{c} denotes the average of c over cross-sections of Γ_a, Γ_v , and ξ is a permeability allowing for transfer/exchange over the interfaces Γ_a, Γ_v between the periarterial and perivenous networks and their surroundings. Moreover, we model the membrane between the parenchyma and the CSF spaces as a semi-permeable membrane with permeability coefficient β_{pia} . For a complete description of this mathematical model and simulation scenarios, see the Supplementary information S1. The initial concentrations in the three-dimensional domain Ω and networks Λ_a, Λ_v are all set to zero.

327 **Intracranial influx after intrathecal injection**

To represent molecular influx into the intracranial compartments following intrathecal injection, without modelling the spinal compartment explicitly, we prescribe a time-dependent molecular influx over the interface towards the spinal CSF compartment with the condition

$$(D\nabla c - \mathbf{u}c) \cdot \mathbf{n} = g_{\text{influx}}, \quad \text{on } \Gamma_{\text{SSAS}}.$$

Here we set

$$g_{\text{influx}}(t) = \frac{m_{\text{tot}}}{T_{\max}^2 |\Gamma_{\text{SSAS}}|} \max(0, T_{\max} - |t - T_{\max}|),$$

328 which expresses a hat-shaped influx function with a peak at T_{\max} and a total tracer injection of m_{tot} (Table 1).

329 **Molecular clearance from the intracranial space and perivascular network ends**

330 We model molecular clearance, into the meningeal lymphatics or other pathways, across the upper, outer (arachnoid) boundary
331 (Figure 1A, Figure 2C), proportional to the concentration in the SAS with a rate constant β_{exit} . We set a no-flux condition at the
332 end nodes of the perivascular networks, not allowing for direct molecular clearance there.

333 **CSF flow in the SAS and ventricular system**

334 We model CSF as an incompressible Newtonian fluid at low Reynolds and Womersley numbers via the Stokes equations
335 with viscosity μ , and account for the convective contribution of the flow induced by CSF production in the choroid plexus.
336 Specifically, we compute the velocity \mathbf{u}_{CSF} and associated pressure p_{CSF} in the SAS and ventricular system induced by a
337 constant production at a rate of u_{in} across the lateral ventricle walls and with efflux across the upper, outer (arachnoid) boundary
338 with efflux resistance R_0 ; and then set $\mathbf{u} = \mathbf{u}_{\text{CSF}}$ in Ω_{CSF} in (1) (Table 1, Figure 2A–E, see also the Supplementary information
339 (S1)). We do not model bulk flow within the brain parenchyma, except within the perivascular network segments extending
340 below the pial surface, and thus set $\mathbf{u} = 0$ in Ω_{PAR} in (1).

341 **Dispersion in the CSF spaces**

342 The pulsatile flow of CSF in the SAS and ventricular system, associated with the cardiac and respiratory cycles, substantially
343 enhances molecular diffusion through dispersion^{42,43,46,77,106,107}. To account for these dispersive effects, while bridging from
344 the pulsatile flow time scale of seconds to a molecular transport time scale of hours, we compute cardiac and respiratory
345 dispersion factors R_c and R_r , both spatially-varying, in Ω_{CSF} (Figure 2A) by combining computational estimates of the
346 respective peak CSF pressure gradients with theoretical estimates for shear-augmented (Taylor) dispersion^{43,106,107} (see
347 Supplementary information S1.3 for a complete description). Combining these effects, we then set $R = R_c + R_r$ and define the
348 effective diffusion coefficient $D = (1+R)D^{\text{Gad}}$ in Ω_{CSF} in (1) in the baseline model.

349 **Perivascular fluid flow induced by CSF pressure differences**

350 To estimate the contribution also to perivascular fluid flow from CSF production, we impose the fluid pressure p_{CSF} induced by
351 CSF production, computed in the SAS and ventricular system, at the end nodes of the periarterial network located within the
352 SAS. For the network end nodes located within the parenchyma, we compute a harmonic extension of the CSF pressure field
353 (by solving a Laplace equation in Ω_{PAR} with p_{CSF} as the boundary value), and set the corresponding value at these end nodes.
354 We then numerically solve a system of hydraulic network equations to compute \hat{u}_a^P defined over Λ_a ; i.e., the pressure-difference
355 induced CSF flow velocity in the periarterial network (see also Supplementary information S1.1.4). We repeat this procedure to
356 compute a corresponding velocity \hat{u}_v^P in the perivenous network Λ_v .

357 **Perivascular fluid flow induced by arterial wall motion**

358 Using the theoretical framework introduced by Gjerde et al.⁴⁰, we also compute analytic estimates for the time-average
359 perivascular flow rate $\langle Q' \rangle$ induced by peristalsis in the arterial network Λ_a ; i.e. the net flow induced by traveling waves
360 of arterial wall motion of frequency f , amplitude ε and wave lengths λ (Figure 3C). The corresponding contribution to the
361 periarterial flow velocity is defined for each segment Λ_i as $\langle Q'_i \rangle / A_i$ where $A_i = \pi(R_2^i - R_1^i)$ is the cross-section area of the PVS
362 segment and $\langle Q'_i \rangle$ is the estimated mean flow rate (see Supplementary information S1.4 for more details). Two wall motion
363 patterns are considered, yielding \hat{u}_a^c and \hat{u}_a^v respectively: *cardiac* pulsations with $f = 1.0\text{Hz}$, $\lambda = 2\text{ m}$ and $\varepsilon = 1\%$ (Figure 3D),
364 and very low-frequency *vasomotion* with $f = 0.1\text{Hz}$, $\lambda = 0.02\text{m}$, and $\varepsilon = 10\%$ (Figure 3E). No flow induced by peristalsis is
365 considered for the perivenous network. In the baseline model, we combine the contributions from CSF production and cardiac
366 peristalsis to set \hat{u} in (1) as $\hat{u}_a = \hat{u}_a^P + \hat{u}_a^c$ in Λ_a , and $\hat{u}_v = \hat{u}_v^P$ in Λ_v .

Parameter	Symbol	Value	Unit	Reference
Extracellular space volume fraction	ϕ_{PAR}	0.2	–	108
Free diffusion coefficient, Gadubutrol	D^{Gad}	3.8×10^{-4}	mm^2/s	109
Parenchymal diffusion coefficient, Gadubutrol	$D^{\text{Gad}}_{\text{PAR}}$	1.2×10^{-4}	mm^2/s	78
Permeability coefficient, pia	β_{pia}	$2.6 \cdot 10^{-8}$	m/s	110
Permeability coefficient, endfoot sheath	ξ_{EF}	$3.8 \cdot 10^{-7}$	m/s	91
Molecular efflux rate	β_{exit}	10^{-4}	mm^2/s	78
Total molecular volume	m_{tot}	0.5	mmol	28
Molecular influx, time-to-peak	T_{max}	1	h	*
CSF production rate	u_{in}	0.63	1 / day	111
CSF viscosity	μ	0.7	$\text{mPa}\cdot\text{s}$	112
CSF outflow resistance	R_0	10^{-5}	$\text{Pa}/(\text{mm}\cdot\text{s})$	78
Dispersion factor, CSF spaces	R	†	–	*

Table 1. Model parameters. †/* denotes computed/estimated within this work.

Description	R_1, R_2	$\xi_{\text{PVS-CSF}}$	$D _{\Omega_{\text{CSF}}}$	$D _{\Omega_{\text{PAR}}}$	$\mathbf{u} _{\Omega_{\text{CSF}}}$	$\hat{u} _{\Lambda_a}$	$\hat{u} _{\Lambda_v}$
baseline	$R_2 = 2R_1$	ξ	$(1+R)D^{\text{Gad}}$	$D^{\text{Gad}}_{\text{PAR}}$	\mathbf{u}_{CSF}	$\hat{u}_a^p + \hat{u}_a^c$	\hat{u}_v^p
no CSF production	–	–	–	–	$\mathbf{0}$	\hat{u}_a^c	0
reduced pulsatility	–	–	$(1+0.1R)D^{\text{Gad}}$	–	–	–	–
increased CSF dispersion	–	–	$(1+10R)D^{\text{Gad}}$	–	–	–	–
higher PVS flow	–	–	–	–	–	$\hat{u}_a^p + \hat{u}_a^c + \hat{u}_a^v$	–
higher PVS exchange	–	100ξ	–	–	–	–	–
dilated PVS	$R_2 = 3R_1$	–	–	–	–	$\tilde{u}_a^p + \tilde{u}_a^c$	–

Table 2. Overview of models and model variations. (– denotes equal to the corresponding baseline value). Each PVS cross-section is modelled as a concentric annulus with inner radius R_1 and outer radius R_2 and such that $R_2 = \beta R_1$. Let ξ denote the astrocytic endfeet permeability estimated by Koch et al.⁹¹. The diffusion coefficients D^{Gad} represent the (free) diffusion coefficient of Gadubutrol in CSF (water), and $D^{\text{Gad}}_{\text{PAR}}$ its effective diffusion coefficient in human cortical tissue, all at body temperature^{76,109}. R is the combined cardiac and respiratory dispersion enhancement field (see Methods). \mathbf{u}_{CSF} is the CSF velocity field induced by CSF production in Ω_{CSF} , and \hat{u}_a^p and \hat{u}_v^p the axial velocity induced in the periarterial and perivenous networks, respectively, by the corresponding pressure differences. \hat{u}_a^c and \hat{u}_a^v is the periarterial velocity induced by arterial pulse wave wall motion and slow vasomotion, respectively. Last, \tilde{u}_a^c and \tilde{u}_a^p are as \hat{u}_a^c and \hat{u}_a^p , respectively, but with dilated PVS.

Model and material parameters

Model and material parameters are summarized in Table 1, and Table 2 gives an overview of the different in-silico scenarios. We assume that the porosity equals the extracellular space volume fraction $\phi = \phi_{\text{PAR}}$ within the parenchyma and $\phi = 1$ elsewhere. The effective diffusion coefficient is set equal to that of Gadubutrol in free water in the PVS networks: $\hat{D} = D^{\text{Gad}}$; weighted by a dispersion factor R in the CSF spaces: $D|_{\Omega_{\text{CSF}}} = (1+R)D^{\text{Gad}}$; and modulated by the porosity and tortuosity ($\lambda = 1.78$) in the parenchyma: $D|_{\Omega_{\text{PAR}}} = D^{\text{Gad}}_{\text{PAR}}$. We set ξ depending on whether the PVS segment is fully embedded within the CSF spaces ($\xi = \xi_{\text{CSF}}$) or parenchyma ($\xi = \xi_{\text{EF}}$), or neither (see also Supplementary information S1). Additionally, we increase the permeability ξ (100×) at the leaf nodes of Λ_a , linearly decreasing to the baseline permeability at the next network node ($\approx 0.4\text{ mm}$), to account for the transition from explicitly resolved PVSs to their unresolved continuation in the CSF spaces and parenchyma.

Numerical approximation, implementation, and verification

We give a concise summary of the numerical approach here (see Supplementary methods for a comprehensive description). To solve (1) numerically, we use the interior penalty discontinuous Galerkin (DG) method with weighted averages and upwinding for the convection term in the 3D domains¹¹³ – to ensure numerical stability and minimize the artificial presence of negative concentration values. For the 1D domain, we use continuous finite element spaces defined over each of the networks and stabilized with numerical diffusion when \hat{u} is non-zero. Note that the 3D–1D coupling in (1) leads to a 3D solution c with low

regularity properties. Thus, one can only expect lower-order error convergence near Λ_a and Λ_v , see the references¹¹⁴ and¹⁰⁵ for the numerical analysis of DG and continuous Galerkin schemes, respectively. However, away from these 1D networks, almost optimal approximation is expected^{115,116}. To numerically solve the Stokes equations to compute the CSF flow velocity and pressure in the ventricular system and SAS, we use finite element spaces that preserve the incompressibility condition on the discrete level¹¹⁷. This requirement is important for numerical stability when subsequently solving (1)¹¹⁸. The spaces we used for the velocity are continuous along the normal direction; continuity of the tangential component is enforced via interior penalty approaches¹¹⁷. Optimal approximation properties are expected for this scheme. These numerical methods were implemented using the FEniCS finite element framework⁷⁹, and the 3D-1D coupling is handled by the extension FEniCSii⁸⁰. The correctness and accuracy of the numerical solutions were verified by a series of numerical verification experiments (see Supplementary information S1.5).

Model validation

As the primary means of model validation, we compare the in-silico predictions of tracer enrichment and clearance against lymphatic MRI studies (Discussion). In addition, we compare auxiliary model quantities (CSF flow rates and pressure differences, dispersion factor estimates, and the shapes and sizes of PVSs) with the current literature (see Supplementary information S2.1).

Acknowledgments

All authors express their gratitude to Prof. Jürgen Reichenbach for generously sharing the multi-modal human MR data, and to Prof. Erlend Hodneland for facilitating this data exchange. M.E.R. acknowledges support from Stiftelsen Kristian Gerhard Jebsen via the K. G. Jebsen Centre for Brain Fluid Research. M.C., R.M., and M.E.R. acknowledge support from the Research Council of Norway (RCN) via grant #324239 (EMIx). Simulations were performed on the Experimental Infrastructure for Exploration of Exascale Computing (eX3), which is financially supported by the RCN under contract 270053. M.K. acknowledges support from the RCN grant #303362. The figures 1A, 1D, 2C, 3C, 5A and 6A were created in Biorender.

Author contributions statement

M.C., M.K, R.M., and M.E.R. conceived and designed the project. M.C., M.K, R.M., and M.E.R. contributed to software development. M.C., M.K, and R.M. conducted the experiments. M.C. analyzed the results and prepared the figures. M.C. M.K. and R.M and M.E.R wrote the manuscript. All authors edited and reviewed the manuscript.

Competing interests

The authors declare no competing interests.

References

1. Rasmussen, M. K., Mestre, H. & Nedergaard, M. The lymphatic pathway in neurological disorders. *The Lancet Neurol.* **17**, 1016–1024 (2018).
2. Harrison, I. F. *et al.* Impaired lymphatic function and clearance of tau in an Alzheimer’s disease model. *Brain* **143**, 2576–2593 (2020).
3. Eide, P. K. *et al.* Plasma neurodegeneration biomarker concentrations associate with lymphatic and meningeal lymphatic measures in neurological disorders. *Nat. communications* **14**, 2084 (2023).
4. Liu, H. *et al.* Lymphatic influx and clearance are perturbed in Huntington’s disease. *JCI Insight* **9** (2024).
5. Xie, L. *et al.* Sleep drives metabolite clearance from the adult brain. *Science* **342**, 373–377 (2013).
6. Eide, P. K., Vinje, V., Pripp, A. H., Mardal, K.-A. & Ringstad, G. Sleep deprivation impairs molecular clearance from the human brain. *Brain* **144**, 863–874 (2021).
7. Eide, P. K. *et al.* Altered lymphatic enhancement of cerebrospinal fluid tracer in individuals with chronic poor sleep quality. *J. Cereb. Blood Flow & Metab.* **42**, 1676–1692 (2022).
8. Miao, A. *et al.* Brain clearance is reduced during sleep and anesthesia. *Nat. Neurosci.* 1–5 (2024).
9. Hauglund, N. L. *et al.* Norepinephrine-mediated slow vasomotion drives lymphatic clearance during sleep. *Cell* **0** (2025).

- 427 10. Iliff, J. J. *et al.* A paravascular pathway facilitates CSF flow through the brain parenchyma and the clearance of interstitial
428 solutes, including amyloid-beta. *Sci. Transl. Med.* **4**, 147ra111 (2012).
- 429 11. Ringstad, G., Vatnehol, S. A. S. & Eide, P. K. Glymphatic MRI in idiopathic normal pressure hydrocephalus. *Brain* **140**,
430 2691–2705 (2017).
- 431 12. Louveau, A. *et al.* Understanding the functions and relationships of the glymphatic system and meningeal lymphatics.
432 *The J. clinical investigation* **127**, 3210–3219 (2017).
- 433 13. Proulx, S. T. Cerebrospinal fluid outflow: a review of the historical and contemporary evidence for arachnoid villi,
434 perineural routes, and dural lymphatics. *Cell. Mol. Life Sci.* **78**, 2429–2457 (2021).
- 435 14. Bohr, T. *et al.* The glymphatic system: Current understanding and modeling. *iScience* **25**, 104987 (2022).
- 436 15. Ringstad, G. *et al.* Brain-wide glymphatic enhancement and clearance in humans assessed with MRI. *JCI insight* **3**
437 (2018).
- 438 16. Eide, P. K., Valnes, L. M., Lindstrøm, E. K., Mardal, K.-A. & Ringstad, G. Direction and magnitude of cerebrospinal
439 fluid flow vary substantially across central nervous system diseases. *Fluids Barriers CNS* **18**, 1–18 (2021).
- 440 17. Eide, P. K., Pripp, A. H., Ringstad, G. & Valnes, L. M. Impaired glymphatic function in idiopathic intracranial
441 hypertension. *Brain communications* **3**, fcab043 (2021).
- 442 18. Lohela, T. J., Lilius, T. O. & Nedergaard, M. The glymphatic system: implications for drugs for central nervous system
443 diseases. *Nat. Rev. Drug Discov.* **21**, 763–779 (2022).
- 444 19. Eide, P. K. *et al.* Clinical application of intrathecal gadobutrol for assessment of cerebrospinal fluid tracer clearance to
445 blood. *JCI insight* **6** (2021).
- 446 20. van Osch, M. J. *et al.* Human brain clearance imaging: Pathways taken by magnetic resonance imaging contrast agents
447 after administration in cerebrospinal fluid and blood. *NMR Biomed.* e5159 (2024).
- 448 21. Rennels, M., Gregory, T. F., Blaumanis, O. R., Fujimoto, K. & Grady, P. A. Evidence for a ‘paravascular’ fluid circulation
449 in the mammalian central nervous system, provided by the rapid distribution of tracer protein throughout the brain from
450 the subarachnoid space. *Brain Res.* **326**, 47–63 (1985).
- 451 22. Zhang, E., Inman, C. & Weller, R. Interrelationships of the pia mater and the perivascular (Virchow-Robin) spaces in the
452 human cerebrum. *J. anatomy* **170**, 111 (1990).
- 453 23. Ichimura, T., Fraser, P. A. & Cserr, H. F. Distribution of extracellular tracers in perivascular spaces of the rat brain. *Brain
454 Res.* (1991).
- 455 24. Carare, R. O. *et al.* Solutes, but not cells, drain from the brain parenchyma along basement membranes of capillaries and
456 arteries: significance for cerebral amyloid angiopathy and neuroimmunology. *Neuropathol. Appl. Neurobiol.* **34**, 131–144
457 (2008).
- 458 25. Foley, C. P., Nishimura, N., Neeves, K. B., Schaffer, C. B. & Olbricht, W. L. Real-time imaging of perivascular transport
459 of nanoparticles during convection-enhanced delivery in the rat cortex. *Ann. Biomed. Eng.* **40**, 292–303 (2012).
- 460 26. Hannocks, M.-J. *et al.* Molecular characterization of perivascular drainage pathways in the murine brain. *J. Cereb. Blood
461 Flow & Metab.* **38**, 669–686 (2018).
- 462 27. van Veluw, S. J. *et al.* Is CAA a perivascular brain clearance disease? A discussion of the evidence to date and outlook for
463 future studies. *Cell. Mol. Life Sci.* **81**, 239 (2024).
- 464 28. Eide, P. K. & Ringstad, G. Functional analysis of the human perivascular subarachnoid space. *Nat. Commun.* **15**, 2001
465 (2024).
- 466 29. Yamamoto, E. A. *et al.* The perivascular space is a conduit for cerebrospinal fluid flow in humans: A proof-of-principle
467 report. *Proc. Natl. Acad. Sci. U. S. A.* **121**, e2407246121 (2024).
- 468 30. Hadaczek, P. *et al.* The “perivascular pump” driven by arterial pulsation is a powerful mechanism for the distribution of
469 therapeutic molecules within the brain. *Mol. Ther.* **14**, 69–78 (2006).
- 470 31. Iliff, J. J. *et al.* Cerebral arterial pulsation drives paravascular CSF–interstitial fluid exchange in the murine brain. *J.
471 Neurosci.* **33**, 18190–18199 (2013).
- 472 32. Bedussi, B., Almasian, M., de Vos, J., VanBavel, E. & Bakker, E. N. Paravascular spaces at the brain surface: Low
473 resistance pathways for cerebrospinal fluid flow. *J. Cereb. Blood Flow & Metab.* **38**, 719–726 (2018).

- 474 33. Mestre, H. *et al.* Flow of cerebrospinal fluid is driven by arterial pulsations and is reduced in hypertension. *Nat. communications* **9**, 4878 (2018).
- 475 34. Boster, K. A. *et al.* Artificial intelligence velocimetry reveals in vivo flow rates, pressure gradients, and shear stresses in murine perivascular flows. *Proc. Natl. Acad. Sci.* **120**, e2217744120 (2023).
- 476 35. Hirschler, L. *et al.* Region specific drivers of cerebrospinal fluid mobility as measured by high-resolution non-invasive MRI in humans. *Res. Sq.* (2024).
- 477 36. Bilston, L. E., Fletcher, D. F., Brodbelt, A. R. & Stoodley, M. A. Arterial pulsation-driven cerebrospinal fluid flow in the perivascular space: a computational model. *Comput. Methods Biomed. Eng.* **6**, 235–241 (2003).
- 478 37. Rey, J. & Sarntinoranont, M. Pulsatile flow drivers in brain parenchyma and perivascular spaces: a resistance network model study. *Fluids Barriers CNS* **15**, 20 (2018).
- 479 38. Daversin-Catty, C., Vinje, V., Mardal, K.-A. & Rognes, M. E. The mechanisms behind perivascular fluid flow. *PLoS One* **15**, e0244442 (2020).
- 480 39. Kedarasetti, R. T. *et al.* Functional hyperemia drives fluid exchange in the paravascular space. *Fluids Barriers CNS* **17**, 52 (2020).
- 481 40. Gjerde, I. G., Rognes, M. E. & Sánchez, A. L. The directional flow generated by peristalsis in perivascular networks—theoretical and numerical reduced-order descriptions. *J. Appl. Phys.* **134** (2023).
- 482 41. Nozaleda, G. L., Coenen, W., Haughton, V. & Sánchez, A. L. Arterial pulsations and transmantle pressure synergetically drive glymphatic flow. *TBA* (2024).
- 483 42. Asgari, M., De Zélicourt, D. & Kurtcuoglu, V. Glymphatic solute transport does not require bulk flow. *Sci. reports* **6**, 38635 (2016).
- 484 43. Sharp, K. M., Carare, R. O. & Martin, B. A. Dispersion in porous media in oscillatory flow between flat plates: applications to intrathecal, periarterial and paraarterial solute transport in the central nervous system. *Fluids Barriers CNS* **16**, 1–17 (2019).
- 485 44. Thomas, J. H. Fluid dynamics of cerebrospinal fluid flow in perivascular spaces. *J. Royal Soc. Interface* **16**, 20190572 (2019).
- 486 45. Kedarasetti, R. T., Drew, P. J. & Costanzo, F. Arterial pulsations drive oscillatory flow of CSF but not directional pumping. *Sci. reports* **10**, 10102 (2020).
- 487 46. Troyetsky, D. E., Tithof, J., Thomas, J. H. & Kelley, D. H. Dispersion as a waste-clearance mechanism in flow through penetrating perivascular spaces in the brain. *Sci. reports* **11**, 4595 (2021).
- 488 47. Martinac, A. D., Fletcher, D. F. & Bilston, L. E. Phase offset between arterial pulsations and subarachnoid space pressure fluctuations are unlikely to drive periarterial cerebrospinal fluid flow. *Biomech. Model. Mechanobiol.* **20**, 1751–1766 (2021).
- 489 48. Damkier, H. H., Brown, P. D. & Praetorius, J. Cerebrospinal fluid secretion by the choroid plexus. *Physiol. reviews* **93**, 1847–1892 (2013).
- 490 49. Steffensen, A. B. *et al.* Cotransporter-mediated water transport underlying cerebrospinal fluid formation. *Nat. communications* **9**, 2167 (2018).
- 491 50. Liu, G. *et al.* Direct measurement of cerebrospinal fluid production in mice. *Cell reports* **33** (2020).
- 492 51. Greitz, D., Franck, A. & Nordell, B. On the pulsatile nature of intracranial and spinal CSF-circulation demonstrated by MR imaging. *Acta Radiol.* **34**, 321–328 (1993).
- 493 52. Wagshul, M. E., Eide, P. K. & Madsen, J. R. The pulsating brain: a review of experimental and clinical studies of intracranial pulsatility. *Fluids Barriers CNS* **8**, 1–23 (2011).
- 494 53. Sweetman, B. & Linniger, A. A. Cerebrospinal fluid flow dynamics in the central nervous system. *Ann. Biomed. Eng.* **39**, 484–496 (2011).
- 495 54. Fultz, N. E. *et al.* Coupled electrophysiological, hemodynamic, and cerebrospinal fluid oscillations in human sleep. *Science* **366**, 628–631 (2019).
- 496 55. Vinje, V. *et al.* Respiratory influence on cerebrospinal fluid flow – a computational study based on long-term intracranial pressure measurements. *Sci. Rep.* **9** (2019).

- 521 56. Causemann, M., Vinje, V. & Rognes, M. E. Human intracranial pulsatility during the cardiac cycle: a computational
522 modelling framework. *Fluids Barriers CNS* **19**, 84 (2022).
- 523 57. Williams, S. D. *et al.* Neural activity induced by sensory stimulation can drive large-scale cerebrospinal fluid flow during
524 wakefulness in humans. *PLoS biology* **21**, e3002035 (2023).
- 525 58. Zimmermann, J. *et al.* Total cerebral blood volume changes drive macroscopic cerebrospinal fluid flux in humans. *bioRxiv*
526 2023–04 (2023).
- 527 59. Weller, R. O. Microscopic morphology and histology of the human meninges. *Morphologie* **89**, 22–34 (2005).
- 528 60. Bedussi, B. *et al.* Paravascular channels, cisterns, and the subarachnoid space in the rat brain: a single compartment with
529 preferential pathways. *J. Cereb. Blood Flow & Metab.* **37**, 1374–1385 (2017).
- 530 61. Pizzo, M. E. *et al.* Intrathecal antibody distribution in the rat brain: surface diffusion, perivascular transport and osmotic
531 enhancement of delivery. *The J. physiology* **596**, 445–475 (2018).
- 532 62. Mestre, H. *et al.* Periarteriolar spaces modulate cerebrospinal fluid transport into brain and demonstrate altered morphology
533 in aging and Alzheimer's disease. *Nat. Commun.* **13**, 3897 (2022).
- 534 63. Møllgård, K. *et al.* A mesothelium divides the subarachnoid space into functional compartments. *Science* **379**, 84–88
535 (2023).
- 536 64. Smets, N. G., van der Panne, S. A., Strijkers, G. J. & Bakker, E. N. T. P. Perivascular spaces around arteries exceed
537 perivenous spaces in the mouse brain. *Sci. Rep.* **14**, 17655 (2024).
- 538 65. Masri, R., Zeinhofer, M., Kuchta, M. & Rognes, M. E. The modelling error in multi-dimensional time-dependent solute
539 transport models. *ESAIM: Math. Model. Numer. Analysis* **58**, 1681–1724 (2024).
- 540 66. Hodneland, E. *et al.* A new framework for assessing subject-specific whole brain circulation and perfusion using
541 MRI-based measurements and a multi-scale continuous flow model. *PLoS computational biology* **15**, e1007073 (2019).
- 542 67. Watts, R., Steinklein, J. M., Waldman, L., Zhou, X. & Filippi, C. G. Measuring glymphatic flow in man using quantitative
543 contrast-enhanced MRI. *AJNR Am. J. Neuroradiol.* **40**, 648–651 (2019).
- 544 68. Causemann, M., Masri, R., Kuchta, M. & Rognes, M. E. Software and data for "In-silico molecular enrichment and
545 clearance of the human intracranial space", DOI: [10.5281/zenodo.1474916](https://doi.org/10.5281/zenodo.1474916) (2025).
- 546 69. Deistung, A., Dittrich, E., Sedlacik, J., Rauscher, A. & Reichenbach, J. R. ToF-SWI: simultaneous time of flight and
547 fully flow compensated susceptibility weighted imaging. *J. Magn. Reson. Imaging: An Off. J. Int. Soc. for Magn. Reson.
548 Medicine* **29**, 1478–1484 (2009).
- 549 70. Schweser, F., Sommer, K., Deistung, A. & Reichenbach, J. R. Quantitative susceptibility mapping for investigating subtle
550 susceptibility variations in the human brain. *Neuroimage* **62**, 2083–2100 (2012).
- 551 71. Reichenbach, J. R. The future of susceptibility contrast for assessment of anatomy and function. *Neuroimage* **62**,
552 1311–1315 (2012).
- 553 72. Deistung, A., Schweser, F. & Reichenbach, J. R. Overview of quantitative susceptibility mapping. *NMR Biomed.* **30**,
554 e3569 (2017).
- 555 73. Smith, A. J. & Verkman, A. S. Going against the flow: Interstitial solute transport in brain is diffusive and aquaporin-4
556 independent. *The J. physiology* **597**, 4421 (2019).
- 557 74. Hladky, S. B. & Barrand, M. A. The glymphatic hypothesis: the theory and the evidence. *Fluids Barriers CNS* **19**, 9
558 (2022).
- 559 75. Betsholtz, C. *et al.* Advances and controversies in meningeal biology. *Nat. Neurosci.* 1–17 (2024).
- 560 76. Syková, E. & Nicholson, C. Diffusion in brain extracellular space. *Physiol. reviews* **88**, 1277–1340 (2008).
- 561 77. Ray, L. A., Pike, M., Simon, M., Iliff, J. J. & Heys, J. J. Quantitative analysis of macroscopic solute transport in the
562 murine brain. *Fluids Barriers CNS* **18**, 55 (2021).
- 563 78. Hornkjøl, M. *et al.* CSF circulation and dispersion yield rapid clearance from intracranial compartments. *Front. Bioeng.
564 Biotechnol.* **10**, 932469–932469 (2022).
- 565 79. Alnæs, M. *et al.* The FEniCS project version 1.5. *Arch. numerical software* **3** (2015).
- 566 80. Kuchta, M. Assembly of multiscale linear PDE operators. In *Numerical Mathematics and Advanced Applications
567 ENUMATH 2019: European Conference, Egmond aan Zee, The Netherlands, September 30-October 4*, 641–650
568 (Springer, 2020).

- 569 81. Balédent, O. Imaging of the cerebrospinal fluid circulation. *Adult hydrocephalus* **256**, 121 (2014).
- 570 82. Gutiérrez-Montes, C. *et al.* Effect of normal breathing on the movement of CSF in the spinal subarachnoid space. *Am. J.*
571 *Neuroradiol.* **43**, 1369–1374 (2022).
- 572 83. Liu, P., Owashi, K., Metanbou, S., Capel, C. & Balédent, O. Using real time phase contrast MRI to investigate CSF
573 oscillations and aqueductal pressure gradients during free breathing. In *ISMRM 2024*, 1189 (2024).
- 574 84. van Veluw, S. J. *et al.* Vasomotion as a driving force for paravascular clearance in the awake mouse brain. *Neuron* **105**,
575 549–561.e5 (2020).
- 576 85. Munting, L. P. *et al.* Spontaneous vasomotion propagates along pial arterioles in the awake mouse brain like stimulus-
577 evoked vascular reactivity. *J. Cereb. Blood Flow Metab.* **43**, 1752–1763 (2023).
- 578 86. Bojarskaite, L. *et al.* Sleep cycle-dependent vascular dynamics in male mice and the predicted effects on perivascular
579 cerebrospinal fluid flow and solute transport. *Nat. communications* **14**, 953 (2023).
- 580 87. Broggini, T. *et al.* Long-wavelength traveling waves of vasomotion modulate the perfusion of cortex. *Neuron* **112**,
581 2349–2367.e8 (2024).
- 582 88. Coenen, W., Zhang, X. & Sánchez, A. Lubrication analysis of peristaltic motion in non-axisymmetric annular tubes. *J.*
583 *Fluid Mech.* **921**, R2 (2021).
- 584 89. Jung, J.-Y., Lee, Y.-B. & Kang, C.-K. Novel technique to measure pulse wave velocity in brain vessels using a fast
585 simultaneous multi-slice excitation magnetic resonance sequence. *Sensors* **21**, 6352 (2021).
- 586 90. Zhang, E., Richards, H., Kida, S. & Weller, R. Directional and compartmentalised drainage of interstitial fluid and
587 cerebrospinal fluid from the rat brain. *Acta neuropathologica* **83**, 233–239 (1992).
- 588 91. Koch, T., Vinje, V. & Mardal, K.-A. Estimates of the permeability of extra-cellular pathways through the astrocyte
589 endfoot sheath. *Fluids Barriers CNS* **20**, 1–18 (2023).
- 590 92. Bown, C. W., Carare, R. O., Schrag, M. S. & Jefferson, A. L. Physiology and clinical relevance of enlarged perivascular
591 spaces in the aging brain. *Neurology* **98**, 107–117 (2022).
- 592 93. Bakker, E. N. T. P. *et al.* Lymphatic clearance of the brain: Perivascular, paravascular and significance for neurodegenerative
593 diseases. *Cell. Mol. Neurobiol.* **36**, 181–194 (2016).
- 594 94. Gokina, N. I., Bevan, R. D., Walters, C. L. & Bevan, J. A. Electrical activity underlying rhythmic contraction in human
595 pial arteries. *Circ. research* **78**, 148–153 (1996).
- 596 95. Vinje, V. *et al.* Human brain solute transport quantified by glymphatic MRI-informed biophysics during sleep and sleep
597 deprivation. *Fluids Barriers CNS* **20**, 62 (2023).
- 598 96. Ulv Larsen, S. M. *et al.* Sleep pressure propels cerebrovascular oscillations while sleep intensity correlates with respiration-
599 and cardiac-driven brain pulsations. *medRxiv* (2024).
- 600 97. von Holstein-Rathlou, S., Petersen, N. C. & Nedergaard, M. Voluntary running enhances glymphatic influx in awake
601 behaving, young mice. *Neurosci. letters* **662**, 253–258 (2018).
- 602 98. Yildiz, S. *et al.* Immediate impact of yogic breathing on pulsatile cerebrospinal fluid dynamics. *Sci. reports* **12**, 10894
603 (2022).
- 604 99. Lundgaard, I. *et al.* Beneficial effects of low alcohol exposure, but adverse effects of high alcohol intake on glymphatic
605 function. *Sci. reports* **8**, 2246 (2018).
- 606 100. Billot, B. *et al.* Robust machine learning segmentation for large-scale analysis of heterogeneous clinical brain MRI
607 datasets. *Proc. Natl. Acad. Sci.* **120**, e2216399120 (2023).
- 608 101. Billot, B. *et al.* Synthseg: Segmentation of brain MRI scans of any contrast and resolution without retraining. *Med. image*
609 *analysis* **86**, 102789 (2023).
- 610 102. Hu, Y., Schneider, T., Wang, B., Zorin, D. & Panozzo, D. Fast tetrahedral meshing in the wild. *ACM Transactions on*
611 *Graph. (TOG)* **39**, 117–1 (2020).
- 612 103. Hladky, S. B. & Barrand, M. A. Regulation of brain fluid volumes and pressures: basic principles, intracranial hypertension,
613 ventriculomegaly and hydrocephalus. *Fluids Barriers CNS* **21**, 57 (2024).
- 614 104. Silversmith, W., Bae, J. A., Li, P. H. & Wilson, A. seung-lab/kimimaro: Zenodo release v1, DOI: [10.5281/zenodo.5539913](https://doi.org/10.5281/zenodo.5539913)
615 (2021).

- 616 105. Laurino, F. & Zunino, P. Derivation and analysis of coupled PDEs on manifolds with high dimensionality gap arising
617 from topological model reduction. *ESAIM: Math. Model. Numer. Analysis* **53**, 2047–2080 (2019).
- 618 106. Taylor, G. I. Dispersion of soluble matter in solvent flowing slowly through a tube. *Proc. Royal Soc. London. Ser. A.
619 Math. Phys. Sci.* **219**, 186–203 (1953).
- 620 107. Watson, E. Diffusion in oscillatory pipe flow. *J. Fluid Mech.* **133**, 233–244 (1983).
- 621 108. Nicholson, C. & Phillips, J. Ion diffusion modified by tortuosity and volume fraction in the extracellular microenvironment
622 of the rat cerebellum. *The J. physiology* **321**, 225–257 (1981).
- 623 109. Valnes, L. M. *et al.* Apparent diffusion coefficient estimates based on 24 hours tracer movement support glymphatic
624 transport in human cerebral cortex. *Sci. reports* **10**, 9176 (2020).
- 625 110. Jørgen N. Riseth, K.-A. M., Timo Koch. Two-compartment modeling of tracer transport in the brain. In Rognes,
626 M. E., Vinje, V., Dokken, J., Valnes, L. M. & Mardal, K.-A. (eds.) *MRI2FEM II: from magnetic resonance images to
627 computational brain mechanics*, DOI: [xxxx/yyy-zzz](#) (Springer, 2025).
- 628 111. Nilsson, C. *et al.* Circadian variation in human cerebrospinal fluid production measured by magnetic resonance imaging.
629 *Am. J. Physiol. Integr. Comp. Physiol.* **262**, R20–R24 (1992).
- 630 112. Bloomfield, I., Johnston, I. & Bilston, L. Effects of proteins, blood cells and glucose on the viscosity of cerebrospinal
631 fluid. *Pediatr. neurosurgery* **28**, 246–251 (1998).
- 632 113. Ern, A., Stephansen, A. F. & Zunino, P. A discontinuous Galerkin method with weighted averages for advection–diffusion
633 equations with locally small and anisotropic diffusivity. *IMA J. Numer. Analysis* **29**, 235–256 (2009).
- 634 114. Masri, R., Kuchta, M. & Riviere, B. Discontinuous Galerkin methods for 3D–1D systems. *SIAM J. on Numer. Analysis*
635 **62**, 1814–1843 (2024).
- 636 115. Masri, R., Shen, B. & Riviere, B. Discontinuous Galerkin approximations to elliptic and parabolic problems with a Dirac
637 line source. *ESAIM: Math. Model. Numer. Analysis* **57**, 585–620 (2023).
- 638 116. Köppl, T., Vidotto, E. & Wohlmuth, B. A local error estimate for the Poisson equation with a line source term. In
639 *Numerical mathematics and advanced applications ENUMATH 2015*, 421–429 (Springer, 2016).
- 640 117. Hong, Q., Kraus, J., Xu, J. & Zikatanov, L. A robust multigrid method for discontinuous Galerkin discretizations of
641 Stokes and linear elasticity equations. *Numer. Math.* **132**, 23–49 (2016).
- 642 118. Cesmelioglu, A. & Rhebergen, S. A compatible embedded-hybridized discontinuous Galerkin method for the Stokes–
643 Darcy-transport problem. *Commun. on Appl. Math. Comput.* **4**, 293–318 (2022).